JOURNAL OF Materials CHEMISTRY

Synthesis, stoichiometry and structure of the quaternary scandium cuprate $Ba_3Cu_3Sc_4O_{12}$ and of 334-phase solid solution members $Ba_3Cu_3Sc_{4-x}In_xO_{12}$ ($0 \leqslant x \leqslant 4$)†

Duncan H. Gregory,*[a] Philip R. Mawdsley,[a] Sarah J. Barker,[a] Wayne Daniell[b] and David P. Weston[c]

[a]*School of Chemistry, University of Nottingham, University Park, Nottingham, UK NG7 2RD. E-mail: Duncan.Gregory@Nottingham.ac.uk*
[b]*Institut für Physikalische Chemie, Ludwig Maximilians Universität München, Butenandtstr. 5-13, Haus E, D-81377 München, Germany*
[c]*School of Mechanical, Materials, Manufacturing Engineering and Management, University of Nottingham, Nottingham, UK NG7 2RD*

Received 1st November 2000, Accepted 22nd December 2000
First published as an Advance Article on the web 5th February 2001

The quaternary scandium cuprate $Ba_3Cu_3Sc_4O_{12}$ has been prepared *via* the high temperature solid state reaction of the respective binary oxides and $BaCO_3$ in air at 950 °C. The cuprate was characterised by powder X-ray diffraction (PXD) and its structure determined for the first time by Rietveld refinement of powder data. Crystallite morphology and metal stoichiometry were examined by SEM/EDAX. Oxygen stoichiometry and thermal behaviour were evaluated by TG/DTA and TPR. $Ba_3Cu_3Sc_4O_{12}$ crystallises with a tetragonal, perovskite-derived structure in space group *I*4/*mcm* ($a = 11.9021(6)$ Å, $c = 8.3962(4)$ Å, $V = 1189.41(10)$ Å^3, $Z = 4$, $c/a = 0.71$), isostructural with $Ba_3Cu_3In_4O_{12}$. $Ba_3Cu_3Sc_4O_{12}$ is paramagnetic at room temperature consistent with Cu(II). In readily substitutes for Sc to form $Ba_3Cu_3Sc_{4-x}In_xO_{12}$ 334-phases continuously to $Ba_3Cu_3In_4O_{12}$ ($x = 4$). Structures of selected members have been determined from PXD data and correlated to the trivalent cation substituent level, x.

Introduction

Since the advent of high temperature superconductivity in perovskite-related cuprates,[1] there has been a drive to investigate copper-containing phases that seemingly meet the structural and chemical requirements perceived as responsible for the superconducting process. It has also been established that the redox chemistry of the cuprates offers potential application in other types of materials and notably as catalysts (*e.g.* for oxidation of ammonia, carbon monoxide and alcohols, *ortho–para* hydrogen conversion and dehydrogenation of methanol).[2,3]

Perovskite related ternary systems based around indates and scandates began to arouse interest in the early 1990s, although they were first investigated earlier.[4–6] These compounds possess many of the structural motifs that one might identify as a requisite for superconductivity when substituted with copper. Moreover, the reduced toxicity of In and Sc relative to heavy metals such as mercury, bismuth, thallium and lead, found in the charge reservoir layers of cuprates with highest T_cs, is undoubtedly attractive in terms of the processing of potential materials. The substitution of copper on to the B site of perovskite-related structures is a strategy which has been successful in producing many new compounds, yet scandium and indium cuprates remain relatively unstudied. Replacement of In or Sc by Cu in $Ba_2In_2O_5$ leads to doubled perovskite substituted phases, $Ba_2In(Sc)_{2-x}Cu_xO_{4+\delta}$, constructed of two $BaIn(Sc)O_{2.5}$ perovskite units in which up to half the trivalent metal is replaced by copper with a concomitant creation of oxygen vacancies.[4,7–9] Under oxidising conditions δ can be increased but compounds remain essentially insulating. Other related materials were investigated at this time, although the characterisation of these quaternary materials is generally not extensive.[6] More recently a number of new indium and scandium cuprates have been reported including $In_2Ba_2CuO_{6-\delta}$ and the $(Y_{1-x}Sc_x)A_2(Cu_{3-y}Fe_y)O_z$ series (A = Ba, Sr) although none of these compounds have been fully structurally characterised.[10,11] Also, scandium analogues of the carbonate-containing cuprate phases of general formula $Ba_4MCu_{2+x}O_y(CO_3)_z$ (M = alkaline earth or rare earth metal), have been reported, *viz.* $Ba_4Sc_xCu_2O_y(CO_3)_{2-x}$.[12] A recent comprehensive survey of the Ba–In–Cu–O system at 930 °C has revealed that other non-stoichiometric ternary and quaternary indate compositions exist that have yet to be fully characterised.[13] Additionally, ternary phases in the Ba–In(Sc)–O system such as $Ba_2In_2O_5$ and $Ba_8In_6O_{17}$ are oxygen and proton ion conductors,[7,14,15] while in the In(Sc)–Cu–O systems $In_2Cu_2O_5$ and $Sc_2Cu_2O_5$ are members of the $R_2Cu_2O_5$ (*e.g.* R = Y, Lu, Er, Tb) family with well-documented low dimensional magnetic properties.[16,17]

Perhaps one of the more interesting quaternary indate phases is $Ba_3Cu_3In_4O_{12}$ (334) first synthesised in 1989 by Aleandri and von Schnering.[18] The authors describe a novel perovskite superstructure containing highly unusual chains of CuO_4 squares, which undergoes an antiferromagnetic transition below 15 K. Independent studies revealed this compound was metallic at room temperature, becoming semiconducting at low temperature.[19] Substitution of scandium for indium, to give nominal $Ba_3Cu_3In_2Sc_2O_{12}$, decreased the resistance of samples at room temperature, whereas replacement of 50% indium with lead in the parent 334 phase took conductivity from the semiconducting to the semimetallic regime.

†Electronic supplementary information (ESI) available: crystallographic details, output for last cycles of refinement, important interatomic distances and angles, and PXD plots for each refinement; TPR and TGA data for the $x = 0$ and $x = 4$ compounds. See http://www.rsc.org/suppdata/jm/b0/b008787o/

 DOI: 10.1039/b008787o

As part of a study concerning the structure of new indium and scandium cuprates and their properties, we report here the synthesis, characterisation and structure determination of the scandate 334 phase $Ba_3Cu_3Sc_4O_{12}$. The thermal behaviour of the Sc and In phases with respect to hydrogen reduction at bulk and surface levels has been studied. Scandium has been progressively replaced by indium in the 334 phase, defining a solid solution $Ba_3Cu_3Sc_{4-x}In_xO_{12}$ ($0 \leqslant x \leqslant 4$) and the changes in crystal structure with indium content, x, have been investigated.

Experimental

Synthesis of $Ba_3Cu_3Sc_4O_{12}$ and members of the $Ba_3Cu_3Sc_{4-x}In_xO_{12}$ solid solution

The quaternary scandate and solid solution members $Ba_3Cu_3Sc_{4-x}In_xO_{12}$ ($x = 0$, 1, 1.5, 2, 2.5, 3, 4) were synthesised by the high temperature solid state reaction of stoichiometric amounts of $BaCO_3$ (99.9%), CuO (99.9%), Sc_2O_3 (99.99%) and/or In_2O_3 (99.99%). The component binary phases were ground, pelleted (approx. dimensions: 1 cm diameter, 0.5 cm thickness) and fired contained in alumina crucibles at 850–950 °C in air for at least 72 h with regrinding every 24 h. Samples were quench-cooled in air to room temperature. For $x > 0$ samples, the volatilisation of In_2O_3 at these reaction temperatures was initially responsible for excess BaO and CuO (and/or ternary phases) impurities in products. This problem was most effectively overcome by adding a *ca.* 10 wt% excess of In_2O_3.

Characterisation by SEM/EDX

The morphology of microcrystalline products was investigated by scanning electron microscopy (SEM) using a Philips XL 30 ESEM-FEG instrument running at 10.0–20.0 kV in ultra-high vacuum mode. Elemental analysis was simultaneously performed by energy dispersive analysis of X-rays (EDX), taking area and point scans of samples.

Thermal analysis

Temperature programmed reduction (TPR) measurements were carried out using a gas mixture of 5% H_2/95% N_2 (flow rates of 1.92 and 38.4 ml min^{-1} for H_2 and N_2, respectively). Parameters for the measurements (mass of reducible sample; gas flow rate; concentration of H_2) were optimised according to Monti and Baiker.[20] The 334-phase samples (40 mg) were purged for 0.5 h at 298 K in N_2 before exposure to the reducing atmosphere, and simultaneous ramping of the temperature (10 K min^{-1}) up to 1200 K. H_2 consumption was measured using a thermal conductivity detector. Scandium oxide (Sc_2O_3), barium carbonate ($BaCO_3$), indium oxide (In_2O_3) and copper(I)/(II) oxides (Cu_2O, CuO) were run as reference materials under the same conditions.

Simultaneous thermogravimetric analysis and differential thermo-analysis (TG/DTA) were carried out using a Netzsch STA 409 microbalance. *Ex-situ* dehydrated γ-Al_2O_3 was employed as a reference material for DTA measurements, with sample and reference temperatures measured by Pt : Sn thermocouples attached to the centre of each ceramic cuvette. The oven and balance compartments were purged with 5% H_2/95% N_2 for 2 h at 298 K before heating, and the measurements carried out using a gas flow of 30 ml min^{-1} and a heating rate of 5 K min^{-1} (up to 1473 K). 334-Phase samples were accurately weighed before and after reduction to confirm the recorded mass loss.

Characterisation and structure determination by powder X-ray diffraction

PXD data were collected using a Philips XPERT θ–2θ diffractometer with Cu Kα radiation. Initially *ca.* 60 min scans were taken of samples over a 2θ range of 5°–80° to assess purity and to determine lattice parameters. Phase purity was assessed by using the Philips IDENTIFY routine which allows access to the ICDD (JCPDS) database. Some $x > 0$ samples contained small amounts of In_2O_3. Also in some cases, weak reflections from minor impurities were present which could not be identified at this stage, but were later ascribed to other ternary or higher phases during the structure determinations (see below). Major phase peaks of each pattern were indexed on a tetragonal unit cell with lattice parameters $a \approx 12$ Å, $c \approx 8.5$ Å using DICVOL91.[21] Lattice parameters were refined by least squares fitting of PXD data. Reflections could be assigned to space group *I*4/*mcm* and patterns were in agreement to those calculated by POWDERCELL 2.3[22] from the model for $Ba_3Cu_3In_4O_{12}$ solved from single crystal X-ray diffraction data.[18]

Structure refinement was performed on data collected for 334-phase samples in the range 5–120° 2θ with a step size of 0.02° 2θ over *ca.* 16 h. The structure of $Ba_3Cu_3Sc_4O_{12}$ was refined by the Rietveld method using the General Structure Analysis System (GSAS) software.[23,24] The Thompson–Cox–Hastings pseudo-Voigt function (peakshape function 3 within GSAS) was used to model peak shape and the background was modelled by an exponential expansion function (background function 6 within GSAS), with 6 refined coefficients, accounting for contributions at both low and high Q. Initial cycles allowed for the variation of the scale factor, zero-point and lattice parameters. As the refinement progressed atomic positions, peak width parameters, profile coefficients and isotropic temperature factors were introduced. Anisotropic temperature factors for metal and non-metal atoms were varied in final cycles but often destabilised the refinement and more often tended to yield negative values for U_{nn}, particularly for oxygen sites. Applying constraints on the oxygen anisotropic temperature factors did not improve the refinement or prevent negative parameters and in final cycles independent isotropic thermal parameters were refined for the three O sites. Additional weak peaks were observed in the profile from the aluminium sample holder. These could not be easily excluded due to problems of overlap with 334-phase reflections. The reflections were adequately handled, in this instance, by refining Al metal as a "secondary phase".

Over the course of the refinement we considered possible non-stoichiometry in existing oxygen sites and potential population of sites reported as vacant in the model of $Ba_3Cu_3In_4O_{12}$ derived from single crystal X-ray data.[18] Considering also our thermogravimetric data, analyses and magnetic data, we were not surprised that attempts to vary occupancy of the three existing sites led to either no deviation from full occupancy or slight increases above unity. The O1, O2 and O3 site populations were therefore left fixed at 100% in final refinement cycles. Negligible features were found in Fourier difference maps and our attempts to refine atom occupancies at positions within the defect perovskite framework—notably the 4d (0, ½, 0) position above and below Cu1 square planes—led to no improvements in the fit, without exception. A disordered model in which the occupancies of the three existing oxygen sites *and* that of the 4d site were allowed to vary gave O1–O3 sites as *ca.* 90% occupied and the 4d site as *ca.* 10% occupied. Residuals improved by approximately 0.1% but all anion temperature factors became negative and this model was discarded. The final ordered model, therefore, is commensurate with a copper(II) scandate in agreement with magnetic data.

Structure refinements of other members of the solid solution

(nominally, $x=1$, 2, 3, 4) were performed following a similar strategy using diffraction data collected under similar conditions. In some cases either constraints were applied to oxygen isotropic thermal parameters or all three U_{iso} parameters were fixed at small positive values. Also, either thermal or occupancy parameters were fixed for the (In, Sc) site (16j: x, 0, ¼) in final cycles in instances where destabilising correlation occurred. For $x>1$ samples additional impurity phases were observed. Aside from In_2O_3 in the $x=4$ sample, which was easily refined as a secondary phase, several weak reflections were observed in indium-rich samples ($x=2$, $x=3$) that could not, at first, be identified. Initial attempts to exclude these peaks met with limited success given the location of the most intense of these over the approximate range $30^\circ \geqslant 2\theta \geqslant 33^\circ$ where the major 334-phase reflections are placed. The patterns of a number of likely ternary and quaternary indate, scandate and cuprate phases were investigated using POWDERCELL 2.3.[22] From generated peak positions and intensity data, $Ba_2In_2O_5$ was initially included as the impurity phase in the $x=3$ sample but the refinement improved dramatically only on inclusion of a doubled-perovskite phase $Ba_2In_{2-x}Cu_xO_{4+\delta}$ (*e.g.* R_{wp} dropped from *ca.* 10% to *ca.* 5%).[6–9] In this sample, the indium cuprate impurity phase parameters were refined until the refinement was stable and convergent and then fixed in final cycles. The $x=2$ sample, by contrast, contained a further 334-phase visible as broadening of peaks at lower 2θ values and resolved peak splitting at higher angles. The 334 impurity phase was fitted to the $x=4$ end-member indate and refined progressively. The impurity phase parameters were fixed in final cycles. The refined sample compositions were thus: $x=0$, 1: phase-pure 334, $x=2$: 85 wt% ($Sc_{0.5}In_{0.5}$) 334, 15 wt% In 334, $x=3$: 92 wt% 334, 8 wt% $Ba_2In_{2-x}Cu_xO_{4+\delta}$, $x=4$: 97 wt% 334, 3 wt% In_2O_3.

Magnetic susceptibility

Magnetic susceptibility experiments were performed at 298 K using a Johnson Matthey magnetic susceptibility balance. Ground samples (*ca.* 0.1 g) were loaded into pre-weighed silica sample tubes. Sample tubes were filled to a height of approx. 1.5 cm. After correction for the diamagnetism of the tubes, Sc ($x=0$) samples gave a value for $\chi_g = 5.3\times10^{-6}$ emu g^{-1} and corresponding $\chi_M = 5.6\times10^{-3}$ emu mol^{-1} (corrected for core diamagnetism) giving a moment of 2.1 μ_B per Cu atom, whereas In ($x=4$) samples gave values of $\chi_g = 5.8\times10^{-6}$ emu g^{-1}, $\chi_M = 7.6\times10^{-3}$ emu mol^{-1} and a corresponding moment of 2.5 μ_B/Cu.

Results and discussion

The 334-phase cuprates, $Ba_3Cu_3Sc_{4-x}In_xO_{12}$, are readily synthesised by high temperature solid state reaction across a solid solution ($0\geqslant x\geqslant 4$) from $Ba_3Cu_3Sc_4O_{12}$ ($x=0$) to $Ba_3Cu_3In_4O_{12}$ ($x=4$). In all cases reactions were complete after *ca.* 72 h, although control of sample homogeneity was difficult, particularly at higher indium ratios where volatilisation of In_2O_3 at the reaction temperature could lead to impurities and off-stoichiometric products. Addition of excess In_2O_3 proved an adequate method of avoiding these problems. Closed vessels were investigated briefly as an alternative to excess In_2O_3 addition and these are currently being examined further with respect to this and other related systems. PXD patterns show a systematic shift to lower 2θ with increasing indium content, x, consistent with an increase in unit cell size. The lattice parameters and cell volumes calculated from the indexing of PXD data for representative samples are shown in Table 1 and Fig. 1. The samples approximately follow Vegard's law for a solid solution with gradual replacement of the trivalent cation. The cell parameters thus increase in a close to linear fashion as smaller Sc^{3+} (0.73 Å) is replaced by larger In^{3+} (0.79 Å) in the octahedral 16j position of the 334 structure.[25]

Table 1 Lattice parameters (from DICVOL91) for representative $Ba_3Cu_3Sc_{4-x}In_xO_{12}$ samples

Sample	Nominal indium content, x	a/Å	c/Å	V/Å^3	c/a
$Ba_3Cu_3Sc_4O_{12}$	0	11.899(2)	8.394(5)	1188(2)	0.71
$Ba_3Cu_3Sc_3InO_{12}$	1	11.951(6)	8.420(6)	1202(3)	0.70
$Ba_3Cu_3Sc_{2.5}In_{1.5}O_{12}$	1.5	11.964(9)	8.429(6)	1207(3)	0.70
$Ba_3Cu_3Sc_2In_2O_{12}$	2	11.989(8)	8.440(8)	1213(3)	0.70
$Ba_3Cu_3Sc_{1.5}In_{2.5}O_{12}$	2.5	12.045(7)	8.469(6)	1229(2)	0.70
$Ba_3Cu_3ScIn_3O_{12}$	3	12.065(3)	8.481(3)	1235(1)	0.70
$Ba_3Cu_3In_4O_{12}$	4	12.121(3)	8.511(4)	1250(2)	0.70

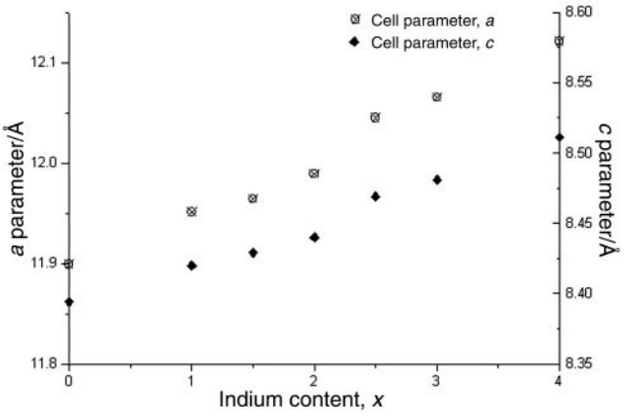

Fig. 1 Plot of lattice parameters, a and c, *vs.* indium content, x, for $Ba_3Cu_3Sc_{4-x}In_xO_{12}$ ($0\leqslant x\leqslant 4$) samples.

Given the defect-perovskite structure of $Ba_3Cu_3In_4O_{12}$ and the redox behaviour of other existing scandium and indium cuprates, we pursued several methods of investigating both the cation and anion stoichiometry and the thermal behaviour of the compounds in a reducing atmosphere. Magnetic susceptibility measurements yielded higher than expected moments for $x=0$ and $x=4$ samples but suggest copper is present as Cu(II) (a typical experimental moment being *ca.* 1.9 μ_B including spin–orbit coupling). These one-temperature measurements however are relatively crude and we will collect SQUID data at variable temperature before interpreting the magnetism further. SEM/EDX was used initially to study the morphology of the 334-phase products and generate an accurate description of the metal stoichiometry. SEM micrographs show that the morphology of 334-phase samples is unremarkable. We investigated the end members ($x=0$, 4) and one intermediate composition ($x=2.5$) and in all cases products are microcrystalline with a particle distribution between *ca.* 5 and 200 μm. A typical micrograph is shown in Fig. 2 for $Ba_3Cu_3Sc_4O_{12}$. EDX point scans across a number of particles and samples confirmed that, uniformly, metals were in a 1 : 1 : 1.3 ratio for all x (*i.e.* Ba : Cu : (Sc,In) of 3 : 3 : 4). In the case of the representative mixed composition the analysis agreed well with the nominal stoichiometry (Sc : In 1.4(1) : 2.6(1) *cf.* nominally 1.5 : 2.5). Oxygen analysis was more approximate but yielded reasonable agreement across a range of samples giving for $x=0$ $Ba_3Cu_3Sc_4O_{12(1)}$ and for $x=4$ $Ba_3Cu_3In_4O_{12.2(5)}$.

The pure scandate ($x=0$) and pure indate ($x=4$) were studied thermally using TPR and TG/DTA. TPR data for the quaternary cuprates contain many of the features observed in the reference runs of binary components. Both the scandate and the indate show several prominent peaks in the TPR profiles. These are defined better in the scandate where a peak with a shoulder is observed with a minimum signal at 576 K

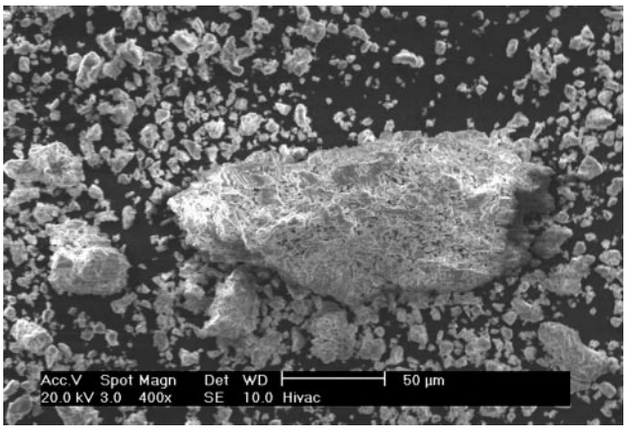

Fig. 2 SEM micrograph of $Ba_3Cu_3Sc_4O_{12}$ crystallites.

followed by a broader peak at 802 K (Fig. 3). The first peak was deconvoluted using a Gaussian fit into two components at 576 and 607 K. These peaks occur in the region where Cu(II) reduces to Cu metal. In a reference TPR run performed on CuO the reduction/adsorption peaks were observed at 618 and 637 K. The broad peak at 802 K in $Ba_3Cu_3Sc_4O_{12}$ approximately corresponds to reduction of Cu(I) to Cu(0). In TPR runs of Cu_2O we observed minima at 743 and 792 K with a very similar broad peak profile. The features observed in the 334-phase cuprate TPR profile are broadly similar to those seen in other alkaline earth metal and lanthanide ternary and quaternary cuprates.[26] Two key points are significant here, however: first the scandate exhibits Cu(II) reduction peaks at temperatures markedly lower than those reported in these other superconducting and non-superconducting cuprates and second the Cu(II) reduction peaks in the 334 material are shifted to lower temperature than those in CuO. These observations suggest that the scandate has a relatively high reducibility among these types of materials. Surface reducibility is dependent on a number of factors besides composition and structure but is, in part, reflective of ease of removal of oxygen from the lattice.[2d] We are currently examining other methods of preparing the 334-phases that should certainly improve particle size and surface area relative to solid state, ceramic synthesis.

TPR runs of $Ba_3Cu_3In_4O_{12}$ contained the same general features seen in the Sc samples, with resolved peaks at 579 and 647 K, a shallow, broad peak at *ca.* 800 K and an additional very broad, shallow peak at 944 K. Rationalising this profile is more open to interpretation. Runs performed on an In_2O_3 standard showed a very broad peak beginning at approximately 700 K and reaching a minimum signal at 1064 K. The peak in the quaternary indate profile is almost certainly related to volatilisation of the indium sesquioxide and was observed again in TG/DTA runs (see below).

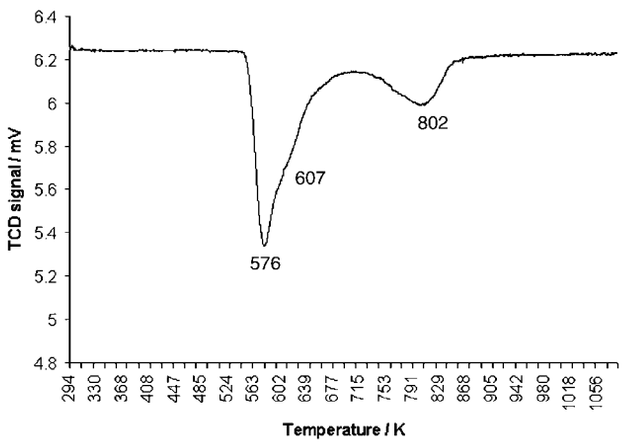

Fig. 3 TPR profile of $Ba_3Cu_3Sc_4O_{12}$, over the range 298 K–1200 K.

TG/DTA data provide several important pieces of information regarding the relative thermal behaviour of the scandate and indate with peaks in the DTA trace and mass loss in the TG profile beginning at *ca.* 350 °C in both the scandate and the indate. The peaks in the DTA trace ostensibly resemble those in the more surface-dependent TPR studies, where peaks at these approximate temperatures correspond to reduction of Cu(II) to Cu(0). TG traces show steady and continuous mass loss in scandate samples until approximately 900 °C at which point the mass loss levels and remains unchanged with increasing temperature. Indate samples, however, show no such levelling of mass loss at high temperature commensurate with volatilisation of the component binary oxide, In_2O_3, following decomposition of the quaternary cuprate. The same effect was observed in TPR traces of In_2O_3 and $Ba_3Cu_3In_4O_{12}$. This volatilisation of In_2O_3 made accurate determination of mass loss approximate at best and ensuing attempts to evaluate oxygen stoichiometry were relatively crude. Mass loss from TGA traces for Sc samples amounted to $\sim$5%. Oxygen stoichiometries calculated from this decomposition of Sc 334 samples to binary oxides and copper (verified by PXD) were in excellent agreement yielding an average value of 12.1(1) which again supports a model in which copper exists as essentially Cu(II) in the quaternary phase.

A number of attempts were made to hold the maximum TG/DTA temperature just below the nominal volatilisation temperature of In_2O_3 (850 °C)[27] to enable calculation of oxygen stoichiometry but at this temperature decomposition/reduction was not complete and "final" mass losses were routinely low (3% *cf.* 5% ideally for $Ba_3Cu_3In_4O_y$, $y \approx 12$). Given the isostructural nature of the indium phase to Sc 334, isovalence of In with Sc and the established structural determination and supporting preliminary magnetic data for $Ba_3Cu_3In_4O_{12}$ in the literature,[18] it seems reasonable to suppose that the two compounds have equivalent levels of oxygen as prepared. This supposition fits well with our analyses, magnetic data and also the results of our structure refinements (detailed below).

Crystallographic data for the structure refinement of $Ba_3Cu_3Sc_4O_{12}$ are presented in Table 2. The fit to the X-ray data is shown in Fig. 4. The refined atomic parameters are listed in Table 3 and important interatomic distances and angles are shown in Table 4. $Ba_3Cu_3Sc_4O_{12}$ is isostructural with $Ba_3Cu_3In_4O_{12}$, crystallising in space group *I*4/*mcm* (No. 140). The tetragonal structure is complex and is considered best in terms of the various metal–oxygen sublattices. A fuller description of this unusual structure type is given in reference 18, and here Aleandri and von Schnering describe

Table 2 Crystallographic data for $Ba_3Cu_3Sc_4O_{12}$

Instrument	Philips Xpert
Radiation; wavelength/Å	Cu Kα; 1.5406, 1.54439
Temperature/K	298
Formula	$Ba_3Cu_3Sc_4O_{12}$
M	974.45
Crystal system	Hexagonal
Space group	*I*4/*mcm* (No. 140)
Z	4
Calculated density, ρ_X/g cm^{-3}	5.442
Unit cell dimensions:	
a/Å	11.9021(6)
c/Å	8.3962(4)
V/Å^3	1189.4(1)
Ratio *c*/*a*	0.705
Observations; parameters	5710; 42
χ^2	2.70
R_{wp}	5.44
R_p	4.06

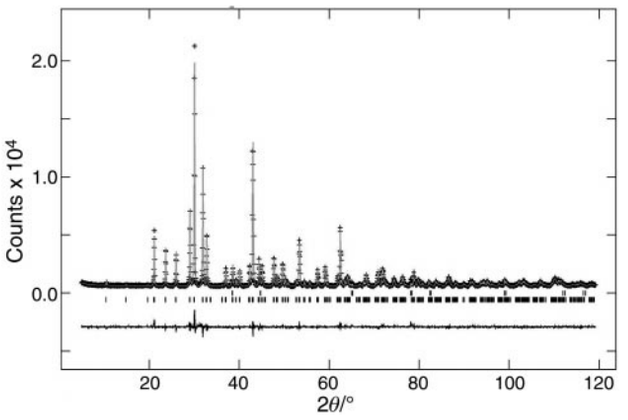

Fig. 4 Final observed (small crosses), calculated (solid line) and difference (below) (OCD) profiles for Rietveld refinement of $Ba_3Cu_3Sc_4O_{12}$.

Table 3 Final atomic parameters for $Ba_3Cu_3Sc_4O_{12}$

Atom	Site	x	y	z	$U_{iso} \times 100$
Ba(1)	4c	0	0	0	0.59(5)
Ba(2)	8h	0.27709(8)	$x+½$	0	0.50(4)
Cu(1)	4b	½	0	¼	0.4(1)
Cu(2)	8h	0.1048(2)	$x+½$	0	1.1(1)
Sc	16j	0.2420(2)	0	¼	0.1(1)
O(1)	16l	0.1201(7)	$x+½$	0.2315(10)	1.2(2)
O(2)	16l	0.1269(7)	x	¼	0.1(1)
O(3)	16k	0.2390(13)	0.5012(5)	0	1.1(1)

$U_{iso} = 4/3[a^2U_{11} + b^2U_{22} + c^2U_{33} + ab(\cos\gamma)U_{12} + ac(\cos\beta)U_{13} + bc(\cos\alpha)U_{23}]$.

the three perovskite-related sub-units, $[BaIn(Sc)O_3]^-$, $[Cu_2In(Sc)O_3]^+$, $[BaCu_{0.5}In(Sc)O_3]$, which make up the constituent slabs of the overall framework. We will consider here, in less detail, the coordination geometry of each metal and how these coordination polyhedra link and interrelate in the overall structure. In its entirety, the structure can be considered to be made up of a network of ScO_6 octahedra connected *via* vertices in three dimensions. Channels exist between these corner-sharing polyhedra which run parallel to the *c*-axis containing either columns of Ba atoms or chains of vertex-sharing CuO_4 square planes. These features of the structure are visualised most simply as a projection along 001 (Fig. 5). Focusing on this representation, two types of row are present running parallel to the 110 direction between lines of ScO_6 octahedra: the first consists only of Ba columns alternately straight and zigzagging in the *c*-direction, the second consists of alternate Ba zigzag

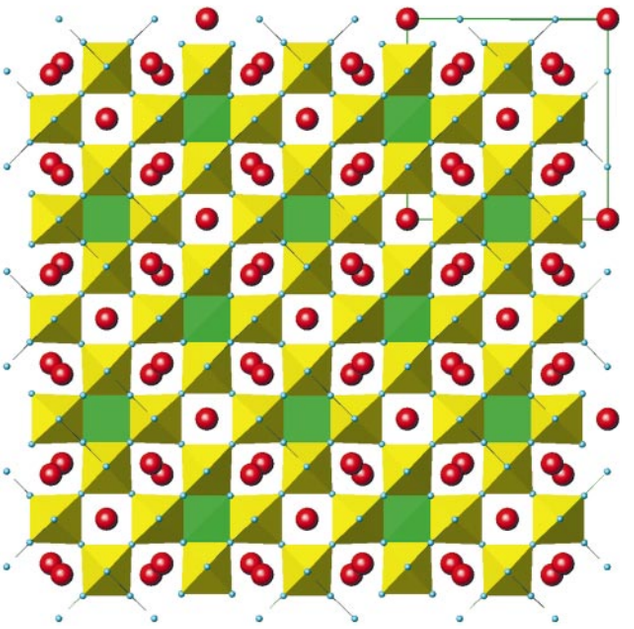

Fig. 5 Structure of $Ba_3Cu_3Sc_4O_{12}$: polyhedral representation projected along the 001 direction, showing corner-linked ScO_6 octahedra, CuO_4 squares (edge-linked to ScO_6 octahedra) and Ba atoms (medium spheres).

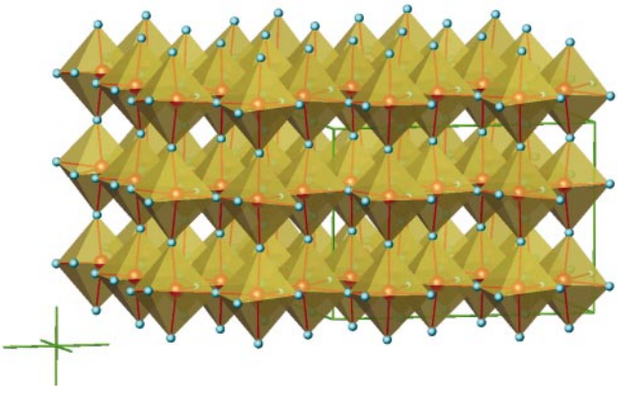

Fig. 6 Structure of the Sc–O sublattice in $Ba_3Cu_3Sc_4O_{12}$ showing layers of corner-sharing ScO_6 octahedra stacked along the 001 direction. Ba and Cu atoms are not shown for clarity.

columns and chains of Cu–O squares. Each Cu–O chain is rotated by 90° in the *ab* plane relative to its predecessor.

Considering now the Sc–O sublattice in isolation (Fig. 6), each ScO_6 octahedron is surrounded by four others in the *ab* plane and

Table 4 Selected interatomic distances and angles in $Ba_3Cu_3Sc_4O_{12}$

Atoms	Distance/Å	Atoms	Angle/°
Ba(1)–O(2) ×8	2.994(8)	O(1)–Cu(1)–O(1)	171.2(5), 90.34(4)
Ba(1)–O(3) ×4	3.107(15)	O(1)–Cu(2)–O(1)	164.9(7)
Ba(2)–O(1) ×2	2.842(9), 3.280(11)	O(3)–Cu(2)–O(3)	165.3(6)
Ba(2)–O(2) ×4	2.985(8)	O(1)–Cu(2)–O(3)	89.04(4)
Ba(2)–O(3) ×2	2.674(7), 3.315(7)	O(1)–Sc–O(1)	82.5(6)
Cu(1)–O(1) ×4	2.028(11)	O(2)–Sc–O(2)	95.6 (6)
Cu(2)–O(1) ×2	1.961(8)	O(3)–Sc–O(3)	167.7(8)
Cu(2)–O(3) ×2	2.018(13)	O(1)–Sc–O(2)	91.2(3), 172.2(5)
$[Cu(2)–O]_{mean}$	1.99(1)	O(1)–Sc–O(3)	81.0(4), 89.7(4)
Cu (1)–Cu (1)[a] ×2	4.1981(2)	O(2)–Sc–O(3)	94.4(3), 93.8(3)
Cu(2)–Cu(2)[b] ×1	3.528(6)	Sc–O(1)–Sc	168.7(5)
Sc–O(1) ×2	2.1818(19)	Sc–O(2)–Sc	174.5(6)
Sc–O(2) ×2	2.0393(16)	Sc–O(3)–Sc	167.7(8)
Sc–O(3) ×2	2.1112(16)		
$[Sc–O]_{mean}$	2.110(2)		

[a]Distance across cavity in *z* direction. [b]Distance across cavity in *x*(*y*) direction.

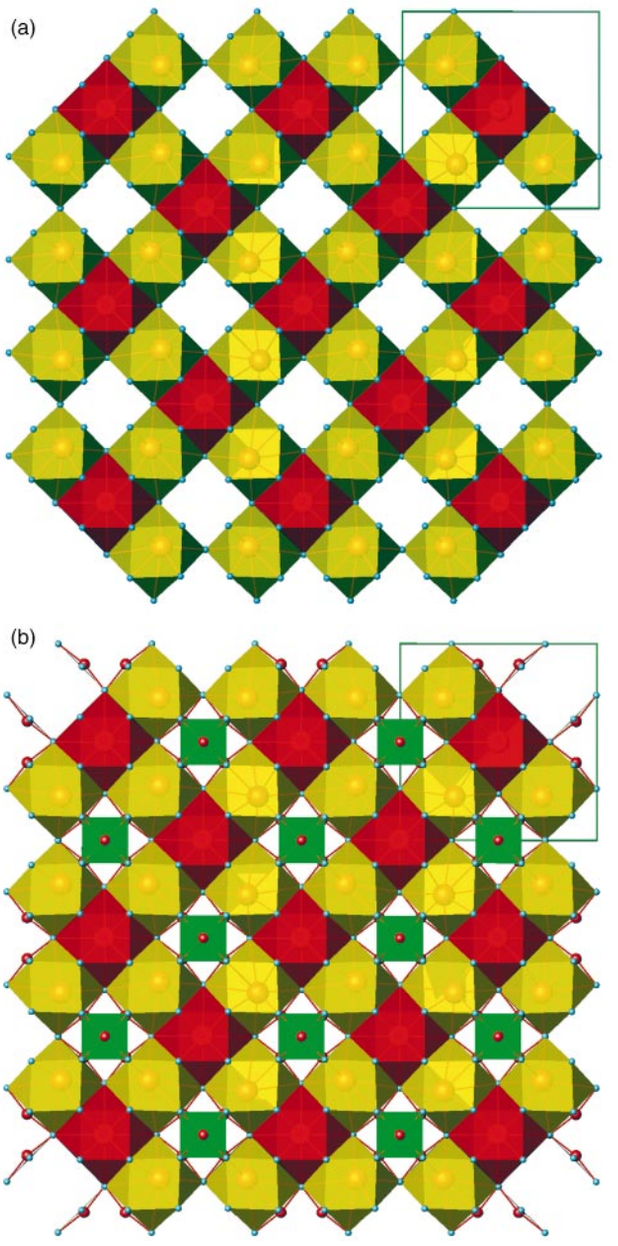

Fig. 7 Structure of the Ba–O sublattice in $Ba_3Cu_3Sc_4O_{12}$ (a) as a polyhedral representation showing only face-sharing Ba–O cuboctahedra, (b) showing also inclusion of Cu–O chains within Ba–O channels.

two above and below along *c*, all linked by vertices. Layers of ScO_6 octahedra hence stack along the *c* direction. This arrangement thus creates the 3D channels occupied by either Ba or Cu–O chains. Each octahedron is quite significantly distorted both axially and in the equatorial plane. Three sets of two equivalent Sc–O bond lengths exist in the octahedron and the two longest distances (Sc–O(1)) and the two shortest distances (Sc–O(2)) lie in the equatorial plane. Coupled with an angular distortion in this plane (reducing the O(1)–O(1) distance relative to the O(2)–O(2) separation), the mismatch in distances leads to a periodic undulation in each Sc–O layer. Similarly, deviation in the O(3)–Sc–O(3) angle from 180° produces zigzag chains of –O–Sc–O– atoms along the 001 direction. The mean Sc–O distance (2.110(2) Å) is comparable with those seen in the few documented barium scandates (*e.g.* $BaSc_2O_4$ where the mean Sc–O distance is 2.12 Å)[28] and the other known quaternary scandium cuprates where Sc is six-coordinate to oxygen (*e.g.* Ba_2ScCuO_4 with a mean Sc–O distance of 2.12(1) Å).[7]

Both barium atoms are coordinated to oxygen in a cuboctahedral geometry, with the bonding environment

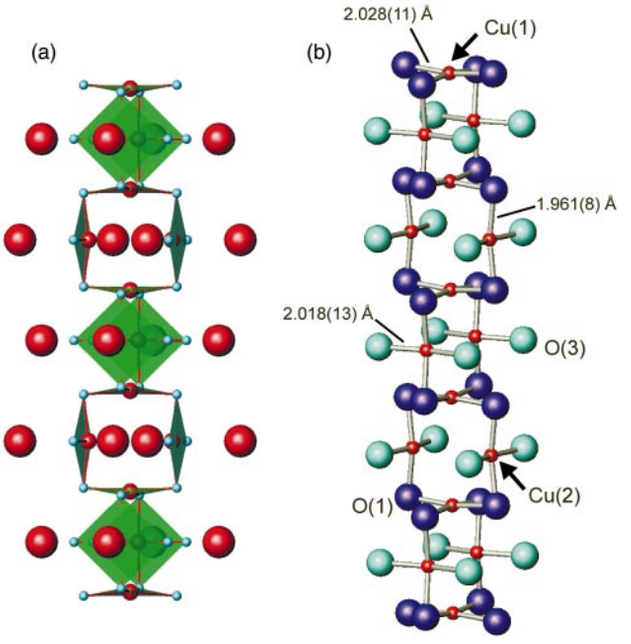

Fig. 8 Detail of chains of CuO_4 planes as (a) a polyhedral representation showing surrounding zigzag columns of Ba atoms, (b) a ball and stick representation showing linking of eight-membered heterocyclic rings.

around Ba(2) more distorted than that of Ba(1). As previously reported for $Ba_3Cu_3In_4O_{12}$, one very short and one very long bond exist between Ba(2) and O(3).[18] The latter Ba(2)–O(3) distance (3.315(7) Å) and the longer of two Ba(2)–O(1) distances (3.280(11) Å) could be regarded as almost non-bonding. As in $Ba_3Cu_3In_4O_{12}$ also, Ba(2) is in close proximity to Cu(2) (2.900(3) Å)—a constraint of the Sc–O 3D framework.[18] The Ba–O cuboctahedra face-share to create a similar, but more condensed, 3D array to that observed in the Sc–O sublattice. Channels again exist running parallel to the 001 direction. The perimeters of these channels are defined by the faces of the Ba(2)–O cuboctahedra (Fig. 7a). These channels are filled by chains of Cu–O square planes. Each Cu(2)–O square (perpendicular to the *ab* plane) shares a face with a Ba–O cuboctahedron and each buckled Cu(1)–O square (approximately parallel to the *ab* plane) shares a vertex, O(1), with each of the four Ba(2)–O cuboctahedra defining the channel edges (Fig. 7b). In each case Ba(2) is repelled away from cuboctahedral faces shared with Cu(2)–O squares. Hence, as the orientation of the square chains rotates by 90 °C along the *c* direction (see below), the Ba–Ba chain zigzags along the 001 direction, alternately towards unshared faces and away from shared faces. Sc atoms sit in the octahedral voids between three Ba–O cuboctahedra and the Cu(1)–O(1) square planes. The Sc–O octahedra thus share faces with Ba–O cuboctahedra and edges with Cu–O squares.

The Cu–O sublattice consists of highly unusual chains of square planar units seen for cuprates, as far as we are aware, only in this structure type. In terms of coordination polyhedra, buckled CuO_4 square planes form vertex-sharing chains in which each square shares two vertices. The chains are constructed such that each Cu–O(1) square (parallel to the *ab* plane) is bridged by Cu–O(2) squares (perpendicular to the *ab* plane) linked *via* opposite O1 corners of the Cu–O(1) square. Each successive pair of Cu–O(2) squares is rotated 90° with respect to its predecessor along the *c* direction (Fig. 8). Hence, this open linked chain could be described loosely as a "paper chain" or "daisy chain" motif. As discussed by Aleandri and von Schnering with respect to $Ba_3Cu_3In_4O_{12}$, the chain could also be described in terms of interconnecting units of eight-membered copper/oxygen rings as a spiroheterocyclic system.[18]

Table 5 Crystallographic data for $Ba_3Cu_3Sc_{4-x}In_xO_{12}$ samples

Nominal In content, x	1	2	3	4
Refined formula	$Ba_3Cu_3Sc_3InO_{12}$	$Ba_3Cu_3Sc_{2.3}In_{1.7}O_{12}$	$Ba_3Cu_3Sc_{0.8}In_{3.2}O_{12}$	$Ba_3Cu_3In_4O_{12}$
M	1047.22	1091.99	1197.85	1253.91
Calculated density, ρ_X/g cm^{-3}	5.7781	5.966	6.217	6.658
a/Å	11.9530(3)	11.9969(3)	12.0719(2)	12.1283(2)
c/Å	8.4211(2)	8.4473(2)	8.4856(2)	8.5106(2)
V/Å^3	1203.15(6)	1215.78(5)	1236.62(4)	1250.96(4)
Ratio c/a	0.705	0.704	0.703	0.702
Observations, parameters	5553, 31	5739, 29	5739, 44	5750, 34
χ^2	3.58	2.13	1.56	1.91
R_{wp}	5.55	4.45	4.45	6.53
R_p	3.98	3.43	3.43	4.94

Table 6 Final atomic parameters for $Ba_3Cu_3Sc_{4-x}In_xO_{12}$ samples ($x>0$)

		$Ba_3Cu_3Sc_3InO_{12}$	$Ba_3Cu_3Sc_{2.3}In_{1.7}O_{12}$	$Ba_3Cu_3Sc_{0.8}In_{3.2}O_{12}$	$Ba_3Cu_3In_4O_{12}$
Ba(1)	U_{iso}[a]	0.61(6)	0.57(5)	0.63(5)	1.22(11)
Ba(2)	x	0.27777(9)	0.27821(8)	0.27909(7)	0.2800(1)
	U_{iso}[a]	0.51(5)	0.56(4)	0.31(5)	0.40(8)
Cu(1)	U_{iso}[a]	0.9(2)	0.7(2)	0.1(1)	0.7(3)
Cu(2)	x	0.1060(2)	0.1059(2)	0.1053(2)	0.1057(3)
	U_{iso}[a]	0.6(1)	0.3(1)	0.2(1)	0.02
(In,Sc)	x	0.2418(1)	0.2417(1)	0.24254(8)	0.2426(2)
	U_{iso}[a]	0.08	0.16	0.01	0.10(4)
In	SOF[b]	0.260(3)	0.421(3)	0.799(4)	1
O(1)	x, z	0.1169(8), 0.230(1)	0.1172(6), 0.226(1)	0.1126(6), 0.225(1)	0.1183(11), 0.232(2)
	U_{iso}[a]	0.1(1)	0.2	0.4(1)	0.02
O(2)	x	0.1297(8)	0.1266(7)	0.1302(7)	0.1289(12)
	U_{iso}[a]	0.1(1)	0.2	0.4(1)	0.02
O (3)	x, y	0.242(1), 0.5005(6)	0.236(1), 0.5020(6)	0.237(1), 0.5036(6)	0.233(2), 0.4986(12)
	U_{iso}[a]	0.1(1)	0.2	0.4(1)	0.02

[a] $\times 100$. [b] Sc $SOF = (1 - \text{In } SOF)$.

Within the overall structure, the chains can be considered as occupying the channels within the Sc–O and Ba–O 3D sublattices. Whichever sublattice framework is considered, each Cu–O chain is rotated by 90° relative to its predecessor along the 110 direction.

Cu(1)–O(1) distances within squares are equal although the plane is buckled such that bridging oxygen atoms (*i.e.* O(1) vertices) are displaced towards Cu(2) in the perpendicularly-linked chains. Cu(2)–O squares, however, are compressed in the c direction (*i.e.* bridging Cu(2)–O(1) < terminal Cu(2)–O(3)) and buckled so that Cu(2) is displaced away from the oxygen plane (the shared face of the Ba(2)–O cuboctahedron) towards the centre of the cavity defined by the eight-membered ring (*i.e.* towards the vacant 4d site). The Cu–O bond lengths we observe are longer than those previously reported for $Ba_3Cu_3In_4O_{12}$ [18] and longer than, for example, the square planar distances in $BaCuO_{2+x}$ (average Cu–O of 1.97 Å).[29] Bond valence calculations using parameters for Cu(II)[30] for the Cu(1) and Cu(2) atoms yielded values of 1.6 and 1.7 respectively. This is probably more indicative of the lack of accuracy in determining the oxygen positions by PXD than a true depiction of oxygen deficiency, which would imply copper oxidation states less than 2.

As anticipated from the appearance and indexing of earlier PXD patterns, intermediate compositions in the nominal $Ba_3Cu_3Sc_{4-x}In_xO_{12}$ series form a solid solution where members are isostructural with the $x=4$ and $x=0$ compounds. The crystallographic data for these compounds ($x=1$, 2, 3, 4)

Table 7 Selected interatomic distances and angles in $Ba_3Cu_3Sc_{4-x}In_xO_{12}$ samples ($x>0$)

	Distance/Å, Angle/°			
Atoms	$x=1$	$x=2$	$x=3$	$x=4$
Cu(1)–O(1) × 4	1.984(13)	1.999(11)	1.934(10)	2.034(19)
$[Cu(2)–O]_{mean}$	2.00(2)	1.96(2)	1.98(2)	2.00(2)
Cu(1)–Cu(1)[a] × 2	4.2105(1)	4.2236(1)	4.2428(1)	4.2553(1)
Cu(2)–Cu(2)[b]	3.585(7)	3.593(6)	3.595(6)	3.623(10)
$[(Sc,In)–O]_{mean}$	2.121(2)	2.131(2)	2.146(2)	2.150(3)
O(1)–Cu(1)–O(1)	170.2(5)	168.4(5)	167(4)	171.5(9)
	94.4(4)	95.2(2)	90.70(6)	90.31(7)
O(1)–Cu(2)–O(1)	169.1(8)	168.6(6)	172.5(6)	167.5(11)
O(3)–Cu(2)–O(3)	165(2)	167(2)	165(2)	165(2)
O(3)–(Sc,In)–O(3)	170.0(7)	165.6(7)	166.9(7)	164(1)
O(1)–(Sc,In)–O(2)	91.23(4)	92.5(3)	92.9(3)	91.0(7)
	169.5(7)	170.0(4)	167.4(4)	170.9(7)
(Sc,In)–O(1)–(Sc,In)	166.1(5)	165.1(4)	161.9(4)	167.9(8)
(Sc,In)–O(2)–(Sc,In)	171.7(8)	174.6(6)	171.5(6)	172.8(11)
(Sc,In)–O(3)–(Sc,In)	169.6(9)	165.5(7)	166.7(7)	164(1)

[a] Distance across cavity in z direction. [b] Distance across cavity in $x(y)$ direction.

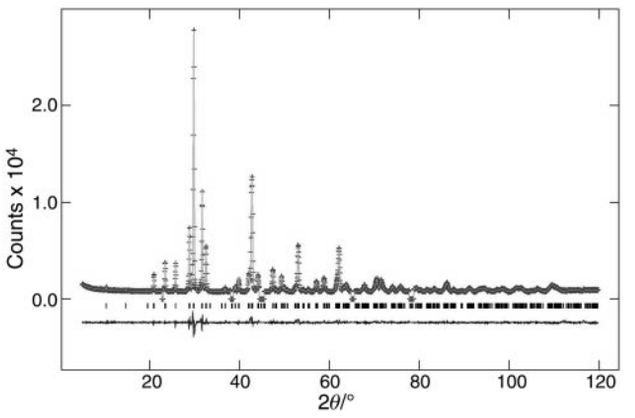

Fig. 9 OCD profile plot for Rietveld refinement of $Ba_3Cu_3Sc_3InO_{12}$.

are presented in Table 5. Atomic parameters and key interatomic distances and angles are shown in Tables 6 and 7 respectively. A representative observed, calculated and difference profile plot is shown in Fig. 9 (for $x=1$). There are several important details and trends that should be highlighted across the series. First in agreement with the trends in lattice parameters seen from indexing, we observe an increase in cell volume with refined composition (*i.e.* indium content, x) that is close to linear. This again conforms to the premise that larger In^{3+} is replacing Sc^{3+} and is responsible for the expansion of the lattice. We also notice a marginal and linear decrease in the *c*/*a* ratio with increasing x (Fig. 10a). This is a reflection of the larger increase in *a* relative to *c* from $x=0$ to $x=4$ which in turn is directly correlated to the anisotropic increase in size of the (Sc,In)–O sublattice in the *ab* plane relative to the *c* direction. This effect is subtle, however, with the (Sc,In)–O equatorial distances in the $(Sc,In)O_6$ octahedron increased by 2% compared to 1.7% for the axial distances. The increase in the

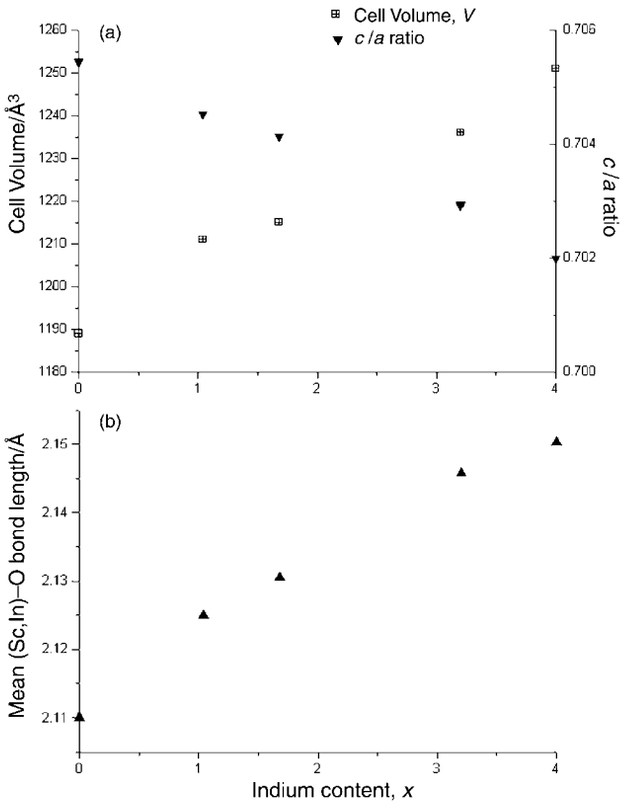

Fig. 10 Plots of (a) cell volume and *c*/*a* ratio and (b) (Sc,In)–O bond length *versus* refined indium content, x, across the $Ba_3Cu_3Sc_{4-x}In_xO_{12}$ solid solution.

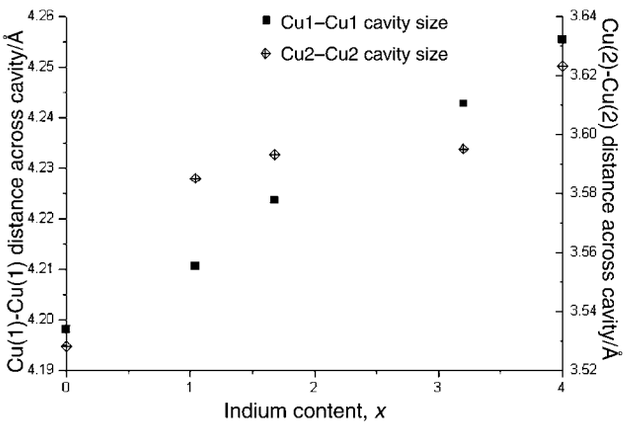

Fig. 11 Plots of size of the 4d cavity (Cu–Cu separations) with x across the $Ba_3Cu_3Sc_{4-x}$ In_xO_{12} solid solution.

mean (Sc,In)–O distance with x is more profound and emphasises that this linear increase is solely responsible for the increase in cell volume (Fig. 10b). Cu–O distances show some scatter with increasing x but are essentially unchanged within standard deviations, as would be expected given the isovalent substitution of Sc by In.

Perhaps the most interesting effect of indium substitution, however, is the increase in the size of the 4d site cavity located in the centre of the heterocyclic Cu–O eight membered rings (Fig. 11). This is most remarkable along the 001 direction where there is an almost linear increase in Cu(1)–Cu(1) separation with x. The Cu(2)–Cu(2) separation (*i.e.* in the *ab* plane) increases less linearly as described by our data. Given that the Cu–O distances remain approximately constant across the solid solution, the increase in 4d cavity volume must be brought about by angular distortion in the Cu–O sublattice. That we see no clear trend in our data regarding the buckling of the Cu–O planes (*i.e.* O(1)–Cu–O(1) and O(1)–Cu(2)–O(1) angles) is again probably a reflection of the inability of PXD techniques to locate accurately the O positions. In principal the Cu(2)–O squares should approach planarity (*i.e.* O(1)–Cu(2)–O(1)→180°) as the (In,Sc)–O sublattice expands. Conversely, the Cu(1)–O squares should become more buckled. In this respect, the angles previously reported for $Ba_3Cu_3In_4O_{12}$ follow this pattern compared to our refined structure of $Ba_3Cu_3Sc_4O_{12}$.[18] The significance of the potential to control this cavity size is at least two-fold. First by increasing the Cu–Cu separations sufficiently it may be possible to at least partially fill the vacant 4d site with oxygen under forcing conditions. Earlier tests on nominal In 334 phase samples indicated metallic conductivity at room temperature.[19] Increased copper oxidation state is of obvious interest with respect to electronic structure and improved electrical conductivity. Conversely, however, it may be of interest to reduce the cavity size with respect to possible magnetic interactions. Preliminary magnetic measurements revealed an antiferromagnetic transition for $Ba_3Cu_3In_4O_{12}$ samples below 15 K.[18] The Cu(2)–Cu(2) separation directly across the 4d cavity is *ca.* 3.6 Å but the Cu(1)–Cu(2) separation between perpendicularly arranged squares (crucially linked by bridging O(1)) is even smaller (*ca.* 2.8 Å). Significantly, both these distances decrease following complete substitution of In by Sc (to *ca.* 3.5 Å and 2.7 Å respectively).

In summary, we have described the synthesis of the 334 quaternary scandate phase, $Ba_3Cu_3Sc_4O_{12}$, and investigated stoichiometry, surface and bulk thermal behaviour under reducing conditions, crystal structure and the substitution chemistry in the $Ba_3Cu_3Sc_{4-x}In_xO_{12}$ solid solution. Measurements on microcrystalline samples indicate paramagnetic behaviour at room temperature with a moment commensurate with a cuprate(II). Our continuing studies of this and other

closely related systems will examine in detail crystal- and magneto-chemistry with appropriate A and B site substitutions and evaluate further the potential catalytic properties of these groups of materials.

Acknowledgements

D. H. G. would like to acknowledge the EPSRC for the award of an Advanced Research Fellowship.

References

1 J. G. Bednorz and K. A. Muller, *Z. Phys. B*, 1986, **64**, 189.
2 See for example: (*a*) M. M. Abou-Sekkina, *Mater. Lett.*, 2000, **42**, 297; (*b*) H. Falcón, M. J. Martinez-Lope, J. A. Alonso and J. L. G. Fierro, *Appl. Catal. B*, 2000, **26**, 131; (*c*) M.-D. Wei, Y. Teraoka and S. Kagawa, *Mater. Res. Bull.*, 2000, **35**, 521; (*d*) R. Sumathi, K. Johnson, B. Viswanathan and T. K. Varadarajan, *Appl. Catal. A*, 1998, **172**, 15; (*e*) I. Halasz, A. Brenner, M. Shelef and K. Y. S. Ng, *J. Catal.*, 1992, **134**, 731.
3 D. Klissurski and V. Rives, *Appl. Catal. A*, 1994, **109**, 1 and references therein.
4 (*a*) W. Kwestroo, H. A. M. van Hal and C. Langereis, *Mater. Res. Bull.*, 1974, **9**, 1623; (*b*) T. A. Kalinina, L. N. Lykova, L. M. Kovba, M. G. Mel'nikova and N. V. Porotnikov, *Russ. J. Inorg. Chem.*, 1983, **28**, 259.
5 See for example: (*a*) K. Mader and Hk. Müller-Buschbaum, *Z. Anorg. Allg. Chem.*, 1985, **528**, 125; (*b*) K. Mader and Hk. Müller-Buschbaum, *Z. Anorg. Allg. Chem.*, 1988, **559**, 89.
6 A. L. Kharlanov, N. R. Khasanova, M. V. Paromova, E. V. Antipov, L. N. Lykova and L. M. Kovba, *Russ. J. Inorg. Chem.*, 1990, **35**, 1741.
7 D. H. Gregory and M. T. Weller, *J. Solid State Chem.*, 1993, **107**, 134.
8 D. H. Gregory and M. T. Weller, *J. Mater. Chem.*, 1994, **4**, 921.
9 T. Shimada, S. Kambe, S. Ohshima, N. Ohnishi and K. Hiraga, *Physica C*, 1997, **282–287**, 935.
10 T. Kijima, H. Sushida, T. Noguchi, M. Yada and M. Machida, *J. Solid State Chem.*, 1997, **131**, 177.
11 Z. Y. Chenl, J. Y. Wang, M. Yu, L. Gao and L. Z. Cao, *J. Alloys Compd.*, 2000, **299**, 107.
12 P. R. Slater and D. S. Wragg, *J. Mater. Chem.*, 1999, **9**, 545.
13 (*a*) R. Horyń, E. Bukowska and A. Sikora, *J. Alloys Compd.*, 2000, **305**, 103; (*b*) R. Horyń, E. Bukowska and A. Sikora, *J. Alloys Compd.*, 2000, **305**, 109.
14 J. B. Goodenough, J. Ruiz-Diaz and Y. S. Zhen, *Solid State Ionics*, 1990, **44**, 21.
15 Y. S. Zhen and J. B. Goodenough, *Mater. Res. Bull.*, 1990, **25**, 785.
16 R. Troć, J. Klamut, Z. Bukowski, R. Horyń and J. Stępień-Damm, *Physica B*, 1989, **154**, 189.
17 M. N. Popova, S. A. Kamin, R. Troć and Z. Bukowski, *Solid State Commun.*, 1997, **102**, 71.
18 L. E. Aleandri and H. G. von Schnering, *J. Less-Common Met.*, 1989, **156**, 181.
19 A. A. Evdokimov, O. A. Skordina, S. A. Smirnov and V. V. Fomichev, *Russ. J. Inorg. Chem.*, 1991, **36**, 463.
20 D. A. M. Monti and A. Baiker, *J. Catal.*, 1983, **83**, 323.
21 (*a*) D. Louer and M. Louer, *J. Appl. Crystallogr.*, 1972, **5**, 271; (*b*) A. Boultif and D. Louer, *J. Appl. Crystallogr.*, 1991, **24**, 987.
22 G. Nolze and W. Kraus, *Powder Diffract.*, 1998, **13**, 256.
23 H. M. Rietveld, *J. Appl. Crystallogr.*, 1969, **2**, 65.
24 A. Larson and R. B. von Dreele, *The General Structure Analysis System*, Los Alamos National Laboratory, 1985.
25 R. D. Shannon and C. T. Prewitt, *Acta Crystallogr., Sect. B*, 1969, **25**, 925.
26 I. Halasz, H.-W. Jen, A. Brenner, M. Shelef, S. Kao and K. Y. S. Ng, *J. Solid State Chem.*, 1991, **92**, 327.
27 *CRC Handbook of Chemistry and Physics*, 61st edn., CRC Press, 1980–81.
28 V. Agafnov, A. Kahn, D. Michel and M. Guymont, *Mater. Res. Bull.*, 1983, **18**, 975.
29 M. T. Weller and D. R. Lines, *J. Chem. Soc., Chem. Commun.*, 1989, 484.
30 I. D. Brown and D. Altermatt, *Acta Crystallogr., Sect. B*, 1985, **41**, 244.